Optimized Tracking of RF Carriers With Phase Noise, Including Pioneer 10 Results

V. A. Vilnrotter, W. J. Hurd, and D. H. Brown
Communications Systems Research Section

The ability to track very weak signals from distant spacecraft is limited by the phase instabilities of the received carrier signal and of the local oscillator employed by the receiver. These instabilities ultimately limit the minimum loop bandwidth that can be used in a phase-coherent receiver, and hence limit the ratio of received carrier power to noise spectral density which can be tracked phase-coherently. This article presents a method for near-real time estimation of the received carrier phase and additive noise spectrum, and optimization of the phase locked loop bandwidth. The method was used with the breadboard DSN Advanced Receiver to optimize tracking of very weak signals from the Pioneer 10 spacecraft, which is now more distant than the edge of the solar system. Tracking with bandwidths of 0.1 Hz to 1.0 Hz reduces tracking signal threshold and increases carrier loop SNR by 5 dB to 15 dB compared to the 3 Hz bandwidth of the receivers now used operationally in the DSN. This will enable the DSN to track Pioneer 10 until its power source fails near the end of the century.

I. Introduction

The ability to track very weak signals from distant spacecraft is limited by the phase instabilities of the received carrier signal and of the local oscillator employed by the receiver. These instabilities ultimately limit the minimum loop bandwidth that can be employed in a phase-coherent receiver, and hence limit the ratio of received carrier power to noise spectral density which can be tracked phase-coherently. To achieve the best performance in a telemetry system, the spectral density of the phase noise should be known, and the parameters of the phase locked loop should be optimized.

At the present time, the Deep Space Network (DSN) uses two distinct operational telemetry receivers. These receivers, designated Block III and Block IV, respectively, employ second order analog carrier tracking loops, with a minimum loop bandwidth of 3 Hz. A 1 Hz bandwidth is possible with the Block IV receiver when tracking 2.3 GHz (S-band) signals, but this bandwidth is seldom used due to receiver oscillator noise, and because of the relatively large phase error caused by the inability of narrow bandwidth second order loops to track dynamics introduced by the rotation of the earth.

One of the important advantages of digital phase locked loops over their analog counterparts is in the flexibility and accuracy of setting and modifying loop parameters. In the DSN Advanced Receiver, which is currently in breadboard form, the loop filter characteristics can be altered in real time. This capability motivates the search for an adaptive algorithm to optimize loop parameters, particularly loop bandwidth, in

real time. Optimization is especially important when tracking weak signals generated by noisy oscillators, such as the signal currently being received from Pioneer 10. When the loop is not stressed by dynamics, or equivalently when the loop order is high enough to track dynamics with negligible phase error, then the optimum loop bandwidth may be defined as that bandwidth which minimizes the steady state rms phase error within the loop. At its optimum value, the loop bandwidth is typically wide enough to track out phase jitter in the received carrier, yet narrow enough to effectively limit the amount of thermal noise allowed into the loop. By reducing the carrier phase jitter, radio loss is reduced and data recovery improved.

In order to optimize loop bandwidth, it is first necessary to model the phase noise properly. The significant components of phase noise are due to the spacecraft transmitter, propagation effects, and VCO noise at the receiver. Spacecraft transmitter noise depends on the mode of transmission, that is, one-way, two-way, or three-way. With one-way transmission, a free running oscillator on the spacecraft determines the transmitted phase. With two- and three-way transmission, the spacecraft phase locks to an uplink signal, multiplies its frequency and phase by a fixed ratio, and uses the resultant as the downlink carrier. If the downlink receiver and uplink transmitter are at the same station, then the mode is termed two-way, while the term "three-way transmission" is reserved for the case when the downlink receiver is at a different station. In the absence of propagation effects, one-way reception is usually dominated by spacecraft oscillator noise, whereas uplink transmitter noise normally dominates two- and three-way reception. A significant propagation effect is that due to solar scintillation, caused by charged particles in the vicinity of the Sun. This effect dominates when the spacecraft is more distant than the Sun, and the Sun-earth-probe (SEP) angle is small. Clearly, all of the above effects depend on a variety of factors; hence any real time characterization of the phase process can be of great value during reception. In this article we present a method for estimating the total phase spectral density in a phase locked receiver, and specifically in the DSN Advanced Receiver. The technique involves measuring the spectral density at the phase detector output, and extracting the individual spectral components by processing the estimated received spectrum. Spectral estimates are obtained by the application of fast Fourier transforms (FFTs) to the phase detector output. Given knowledge of the closed loop transfer function, the phase spectrum, receiver noise spectrum, and received carrier power can all be estimated. The optimum loop bandwidth is determined from these estimated components. Analytic expressions are derived for the case when the phase noise spectral density varies as $f^{-\alpha}$, a model often quoted in the literature. With α equal to three, the model can be used to describe oscillator phase spectra at low frequencies, while for solar scintillation spectra a value of $\alpha = 8/3$ is appropriate.

Finally, we present measurements of phase spectra, and determine optimum loop bandwidths for Pioneer 10 telemetry. Data for both one-way and three-way transmissions are included. It is shown that the Advanced Receiver can reduce the minimum tracking threshold for Pioneer 10 by as much as 5 dB to 15 dB compared to the tracking threshold of current operational receivers. This is accomplished by using 0.1 Hz to 1.0 Hz loop bandwidths, compared to the 3 Hz bandwidths currently used operationally.

II. Mathematical Models

In the following development, we assume that the received signal is of the form

$$s(t) = \sqrt{2}\, A \cos(\omega_0 t + \theta(t) + \psi)$$

where A is the signal amplitude, ω_0 is the carrier radian frequency, $\theta(t)$ is a random phase process, and ψ is a random initial phase. Multiplication by $\sqrt{2}$ has the advantage that the total carrier power becomes $P_c = A^2$, and the slope of the phase detector S-curve near the origin becomes A. This signal representation also allows direct comparison between the baseband phase spectral densities within the phase locked loop and their RF counterparts, where oscillator phase spectra are generally measured. Since in the current application the signal amplitude remains essentially constant for long periods of time (and hence can be estimated with great accuracy), we assume that A is known.

A. Derivation of Observation and Phase Error Spectra

A linear model of the carrier loop is shown in Fig. 1. This model is accurate when the loop is locked, and operating with small rms phase errors. Under these conditions, the loop is continuously generating estimates of the received phase process $\theta(t)$, denoted $\hat{\theta}(t)$, and subtracting the estimate from the received phase. The resulting phase error process $\phi(t) = \theta(t) - \hat{\theta}(t)$ is multiplied by the slope of the phase-detector S-curve at zero frequency (in our case that value is "A"), and filtered by the loop filter in the presence of additive receiver noise $n(t)$. The output of the loop filter is an error process $e(t)$ which is used to control the frequency of the voltage-controlled oscillator (VCO), or the equivalent numerically controlled oscillator (NCO) typically employed in digital loops. Instabilities within the receiver VCO are modeled as an additive phase process $\psi_r(t)$ that is added to the VCO output. At this point it is useful to introduce the Heaviside differential operator $p = d/dt$, which allows relating the output "z" of a linear filter to its input "x" in the time domain as $z(t) = F(p)\, x(t)$, where $F(p)$ is a ratio of polynomials in p. The

transfer function of the filter in the frequency domain becomes $F(j\omega) = F(p)|_{p=j\omega}$. (Subsequently we shall use both radian frequency ω and frequency $f = \omega/2\pi$, as appropriate.) Suppressing time dependence and making use of the Heaviside differential operator, the loop equations can be expressed as

$$\phi = \theta - \hat{\theta} \tag{1a}$$

$$y = A\phi + n \tag{1b}$$

$$x = KG\left\{\frac{F(p)}{p}\right\} y \tag{1c}$$

$$\hat{\theta} = x + \psi_r \tag{1d}$$

where K is the filter gain, G the VCO gain, and y the noise-corrupted observable. In general, the received phase consists of phase processes due to modulation, doppler, and transmitter VCO instabilities. Any initial phase offsets are assumed to have been tracked out by the receiver. For the type of signals typically observed by the Advanced Receiver, the use of subcarriers can be assumed, which implies that modulation sidebands are far removed from the carrier and hence may be ignored. Therefore, the received phase can be modeled as $\theta = d + \psi_t$ where d is due to possible doppler rates and ψ_t describes the effects of additive transmitter VCO instabilities. Defining the transceiver phase process $\Delta\psi = \psi_t - \psi_r$ and letting $B(p) = KGF(p)/p$, Eqs. (1a), (1c), and (1d) can be used to obtain

$$\hat{\theta} = B(p)\,y + \psi_r = AB(p)\,\phi + B(p)\,n + \psi_r \tag{2a}$$

$$\phi = d + \Delta\psi - AB(p)\,\phi - B(p)\,n \tag{2b}$$

or

$$\phi = \left\{\frac{1}{1+AB(p)}\right\}(d+\Delta\psi) - \left\{\frac{AB(p)}{1+AB(p)}\right\}\frac{n}{A} \tag{3a}$$

$$y = A\left\{\frac{1}{1+AB(p)}\right\}(d+\Delta\psi) + \left\{\frac{1}{1+AB(p)}\right\} n \tag{3b}$$

Since the closed-loop transfer function of the loop is

$$H(j\omega) = \frac{AB(j\omega)}{(1+AB(j\omega))} \tag{4}$$

the power spectral densities of the observation and phase error processes can be represented as

$$S_\phi(f) = |1 - H(j2\pi f)|^2\, S_\zeta(f) + |H(j2\pi f)|^2\, \frac{S_n(f)}{A^2} \tag{5a}$$

$$\frac{S_y(f)}{A^2} = |1 - H(j2\pi f)|^2\, S_\zeta(f) + |1 - H(j2\pi f)|^2\, \frac{S_n(f)}{A^2} \tag{5b}$$

where $\zeta = d + \Delta\psi$. If the doppler and transceiver phase processes are independent, then $S_\zeta(f) = S_d(f) + S_{\Delta\psi}(f)$. Note that in Eq. (5b) we divided both sides of the equation by A^2 in order to emphasize the similarities between the observation and phase error spectra, when both are expressed in the same units. Aside from a scaling factor, the only difference between the two equations is that the additive noise component in the phase error process is filtered by $H(j2\pi f)$, whereas in the observation process it is effectively filtered by $(1 - H(j2\pi f))$.

Now let us consider the received phase process, specifically in the case where d is small. The received phase spectrum then depends on the transmitted phase spectrum and on the properties of the channel. The free space channel is generally considered to be an additive white Gaussian noise channel which does not introduce phase distortion. For now we will neglect the effects of the sun and the solar corona on the received phase spectrum, as these will be discussed in a later section. Therefore, in this case the phase stability of the received carrier is dominated by the phase stability of the transmitted carrier. Two transmission modes commonly used in the DSN will be examined in this analysis.

In the one-way mode, the spacecraft oscillator is the source of the transmitted carrier. The term one-way stems from the notion of the frequency reference traveling only one way, from the spacecraft to the ground station. In the one-way mode, the phase noise spectrum is normally dominated by a term varying as inverse f^3, for frequencies very close to the carrier.

The other transmission mode discussed here is known as three-way transmission. In this mode, a carrier reference is transmitted to the spacecraft from a ground station. The spacecraft receiver phase locks to this signal, multiplies the frequency by a known ratio, and uses the resultant as the downlink frequency. Thus the received phase depends on the phase characteristics of the uplink oscillator and of the spacecraft phase locked loop. In our experiments with the Pioneer 10 spacecraft, transmission in the two-way mode is not feasible since the round trip light time is roughly 11 hours 30 minutes, so that by the time the transmitted reference is returned

by the spacecraft, the transmitting antenna is on the other side of the world.

For three-way telemetry, the received process spectrum cannot be described by a simple inverse f^3 model, in general. Now the effects of the transmitter tracking loop on the uplink spectrum must be properly taken into account. A linear model of the tracking loop on the spacecraft appears in Fig. 2. This model is similar to the one describing the receiver tracking loop, except that now the loop's output is its estimate of the uplink phase. The subscript "t" denotes "transmitter," distinguishing the components of this loop from those of the receiver. The transmitter loop tracks the uplink phase, using it as the reference for the downlink telemetry. Thus, the phase of the downlink carrier is identical to the loop's estimate of the uplink phase. The power spectral density of the downlink transmitted phase process θ_t can be derived with the same techniques used to derive the spectral density of the receiver phase process. The result is

$$S_{\theta_t}(f) = |H_t(j2\pi f)|^2 \left[S_{\theta_u}(f) + \frac{S_{n_t}(f)}{A^2} \right]$$

$$+ |1 - H_t(j2\pi f)|^2 \; S_{\psi_t}(f) \qquad (5c)$$

where θ_u is the random phase of the uplink oscillator multiplied by the spacecraft transponder ratio. Note that the uplink phase process and the internal noise are both filtered by the closed loop transfer function, while the transmitter's phase process is effectively filtered by the complementary filter function $(1 - H(j2\pi f))$. In our case $S_{\theta_u} \cong 10^{-3}\, S_{\psi_t}$, but $|1 - H_t(j2\pi f)|^2 \lesssim 10^{-4}$ at the low frequencies of interest, so that typically S_{θ_u} is the dominant component of the downlink phase process.

The transmission channel may also affect the spectral purity of the carrier phase. A good example of a prominent channel effect is provided by the solar corona [1]. The resulting phase degradation can be appreciable, often negating the benefits of highly stable earth-based oscillators operating in three-way mode. The power spectrum of the phase degradation for this solar effect is typically inversely proportional to the 8/3 power of frequency.

B. Closed Loop Transfer Function and Its Effects

Next we examine the structure of the closed-loop transfer function in greater detail, and consider its effects on various phase process and additive noise models.

The Advanced Receiver employs second and third order loops. Approximating the rapidly sampled data loop by a continuous time loop, the transfer functions of the loop filter and of the resulting closed loop for a third order, type III loop are [2]

$$F(s) = \frac{1 + \tau_2 s}{\tau_1 s} + \frac{1}{\tau_2 \tau_3 s^2} \qquad (6a)$$

$$H(s) = \frac{r(k + \tau_2 s + (\tau_2 s)^2)}{r\,(k + \tau_2 s + (\tau_2 s)^2) + (\tau_2 s)^3} \qquad (6b)$$

where τ_1, τ_2, τ_3 are constants, $r = Ak\tau_2^2/\tau_1$, $k = \tau_2/\tau_3$ and s is the Laplace transform variable. The steady-state transfer function is obtained by letting $s = j\omega$ in Eq. (6b), yielding

$$H(j\omega) = \frac{r\left(k - \frac{\omega^2 g^2}{B_L^2}\right) + \frac{j\omega g r}{B_L}}{r\left(k - \frac{\omega^2 g^2}{B_L^2}\right) + j\left(\frac{\omega r g}{B_L} - \frac{\omega^3 g^3}{B_L^3}\right)} \qquad (7a)$$

$$1 - H(j\omega) = \frac{-j\,\frac{\omega^3 g^3}{B_L^3}}{r\left(k - \frac{\omega^2 g^2}{B_L^2}\right) + j\left(\frac{\omega r g}{B_L} - \frac{\omega^3 g^3}{B_L^3}\right)} \qquad (7b)$$

where

$$g \triangleq B_L \tau_2 = \frac{r}{4}\left(\frac{r - k + 1}{r - k}\right) \qquad (8)$$

These transfer functions can also be expressed in terms of the normalized radian frequency $\tilde{\omega} = \omega / B_L$, indicating that B_L simply scales the frequency variable. Note that the loop reduces to a second order type II loop when $k = 0$. The squared magnitudes of the transfer functions defined in Eq. (7) are of fundamental importance in determining loop performance. These functions are

$$F_1(\tilde{\omega}) \triangleq |H(j\omega)|^2_{\omega = B_L \tilde{\omega}} = \frac{r^2(k - \tilde{\omega}^2 g^2) + \tilde{\omega}^2 (gr)^2}{r^2(k - \tilde{\omega}^2 g^2)^2 + (\tilde{\omega} r g - \tilde{\omega}^3 g^3)^2} \qquad (9a)$$

$$F_2(\tilde{\omega}) \triangleq |1 - H(j\omega)|^2_{\omega = B_L \tilde{\omega}} = \frac{\tilde{\omega}^6 g^6}{r^2(k - \tilde{\omega}^2 g^2)^2 + (\tilde{\omega} r g - \tilde{\omega}^3 g^3)^2} \qquad (9b)$$

Plots of these functions are shown in Fig. 3 for $r = 4$, and $k = 0.0$ and 0.25. Note that for $k \leqslant 0.5$ and $r \geqslant 2$, $F_2(\tilde{\omega})$ is a monotone increasing function of $\tilde{\omega}$, which implies that $B_{L2} > B_{L1}$, $F_2(\omega/B_{L1}) > F_2(\omega/B_{L2})$. This property can be used to establish the existence of an optimum loop bandwidth.

C. Oscillator Phase Noise

Oscillator phase noise can be modeled as [3]

$$S_\psi(f) = \begin{cases} \dfrac{S_1}{|f|^3} + \dfrac{S_2}{f^2} + S_3 & |f| \leqslant F_u \\ \dfrac{S_4}{f^4} & |f| > F_u \end{cases} \tag{10}$$

where F_u is an upper frequency cutoff and the S_i, $i = 1, 4$, are constants. For our interest, we observe that if the transmitter and receiver oscillators are running independently, then their spectral densities add, yielding $S_{\Delta\psi}(f) = S_{\psi_t}(f) + S_{\psi_r}(f)$. Each component is typically of the form given in Eq. (10), although the corresponding constants may be different for the two oscillators. The low-frequency behavior of an oscillator is usually dominated by "frequency flicker noise" [4], giving rise to the well known inverse f^3 behavior of phase fluctuations. Assuming that in the region of interest frequency flicker noise dominates, and further assuming negligible doppler contribution, the power spectral density of the phase process for one-way telemetry can be modeled as

$$S_\xi(f) \cong \frac{S_1}{|f|^3} \tag{11}$$

This model may also be applied to three-way telemetry, if the spacecraft loop bandwidth is so great that the uplink phase process term dominates.

At low frequencies the additive receiver noise is generally white. Denoting its single-sided spectral level by N_0 yields the representation

$$S_n(f) \cong \frac{N_0}{2} \tag{12}$$

With these approximations, the process, additive noise, and observation spectral densities appear as in Fig. 4, for a third order loop with parameters as before.

Note that for filter functions of the form defined in Eq. (7) and inverse f^3 phase processes, the peak of the process spectrum always occurs at a frequency that is a linear function of the loop bandwidth. This can be established by differentiating $|1 - H(j\omega)|^2 S_\xi(f)$ with respect to ω and setting the result equal to zero. The maximum occurs at frequency $f = f^*$, where

$$f^* = C_0(r, k) B_L \tag{13}$$

(the derivation is shown in the Appendix). For ($r = 4, k = 0.25$), $f^* = 0.127\ B_L$; for a second order loop with parameters ($r = 4$, $k = 0.0$), $f^* = 0.147\ B_L$. This result can be used to establish whether or not an observed phase process is adequately described by the f^{-3} model.

D. Optimization of Tracking Loop Bandwidth

The performance of phase-locked loops can be assessed in terms of the total rms phase error σ_ϕ present in the loop. The total mean-squared phase error is the integral of the phase error spectral density defined in Eq. (5a):

$$\sigma_\phi^2 = 2 \int_0^\infty S_\phi(f)\, df \triangleq \sigma_\xi^2 + \sigma_n^2 \tag{14}$$

The components of the total phase error σ_ξ^2 and σ_n^2 are defined as

$$\sigma_\xi^2 = 2 \int_0^\infty |1 - H(j\,2\pi f)|^2 S_\xi(f)\, df \tag{15a}$$

and for white noise spectra of the form $S_n(f) = N_0/2$,

$$\sigma_n^2 = 2\left(\frac{N_0}{2A^2}\right) \int_0^\infty |H(j\,2\pi f)|^2\, df = \left(\frac{N_0}{2A^2}\right) 2B_L \tag{15b}$$

Note that for white noise the spectral level is constant; hence the component of the variance due to white noise increases linearly with loop bandwidth. The process component depends on the power spectrum of the phase, which is generally not constant. However, since the power spectral density is a nonnegative function of frequency, it follows that for $B_{L2} > B_{L1}$, $S_\xi(\omega)\, F_2(\omega/B_{L1}) > S_\xi(\omega)\, F_2(\omega/B_{L2})$. Since this inequality also holds for the integral, the component of the variance due to process noise is a decreasing function of loop bandwidth, for all valid power spectral density functions. It follows from the above argument that a loop bandwidth exists which minimizes the total mean squared phase error.

Loop bandwidth optimization can be achieved for arbitrary phase spectra by computing estimates of the total phase error as a function of loop bandwidth, and selecting the bandwidth

corresponding to the minimum of this function. For the case of additive white receiver noise, this requires knowledge of the parameter $N_0/2A^2$, and of the function $|1 - H(j\,2\pi f)|^2\, S_\xi(f)$, which is the integrand in Eq. (15a). If the power spectral density of the observable and the density of the signal level A are known, then the required integrand can be determined from Eq. (5b):

$$|1 - H(j\,2\pi f)|^2\, S_\xi(f) = \frac{S_y(f)}{A^2} - |1 - H(j\,2\pi f)|^2 \left(\frac{N_0}{2A^2}\right) \tag{16}$$

A major simplification in the optimization algorithm results if the phase process spectrum is assumed to be of the form $f^{-\alpha}$. This assumption is normally valid for one-way transmission, and may be accurate for three-way transmission as well, provided that the instability is dominated either by uplink oscillator or solar scintillation phase noise. Introducing the change of variables $\tilde{f} = f/B_L$, it follows that

$$\sigma_\xi^2 = 2\,S_1 B_L^{(1-\alpha)} \int_0^\infty |1 - H(j\,2\pi\tilde{f})|^2\, \tilde{f}^{-\alpha}\, d\tilde{f}$$

$$= 2\,S_1\, \gamma_0(\alpha) B_L^{(1-\alpha)} \tag{17}$$

where $\gamma_0(\alpha)$ is the value of the integral. Using numerical integration, we found that $\gamma_0(3) = 9.08$ and $\gamma_0(8/3) = 5.87$ for a third order loop with parameters $r = 4$, $k = 0.25$ and a loop bandwidth of 1 Hz.

For the $f^{-\alpha}$ model, the minimum of the total phase error variance can be found by differentiating σ_ϕ^2 with respect to B_L, setting the result equal to zero, and solving for the optimum loop bandwidth B_L^*:

$$\frac{\partial \sigma_\phi^2}{\partial B_L} = -2(\alpha - 1)\, S_1\, \gamma_0(\alpha) B_L^{-\alpha} + 2\left(\frac{N_0}{2A^2}\right) = 0 \tag{18a}$$

yields

$$B_L^* = \left\{ \frac{(\alpha - 1)\, S_1\, \gamma_0(\alpha)}{\dfrac{N_0}{2A^2}} \right\}^{1/\alpha} = \left\{ \frac{(\alpha - 1)\, \sigma_\xi^2}{\sigma_n^2} \right\}^{1/\alpha} B_L \tag{18b}$$

Figure 5 shows the behavior of σ_ξ^2 and σ_n^2 as a function of loop bandwidth, as well as their sum, for $\alpha = 3$ and parameter values $S_1 = 4\pi \times 10^{-4}$ and $(N_0/2A^2) = 2 \times 10^{-2}$. This algorithm for loop bandwidth optimization requires only knowledge of σ_ξ^2, σ_n^2, and the bandwidth at which the measurements were made. Measurement of σ_ξ^2 also allows determination of the phase process constant S_1, via the equation

$$S_1 = \frac{\sigma_\xi^2\, B_L^{(\alpha-1)}}{2\,\gamma_0(\alpha)} \tag{19}$$

In a practical system, the required parameters and spectral densities are not known and hence must be estimated. The accuracy of the predictions ultimately depends on the accuracy of the estimates. The choice of best estimator structure often depends on the application. The selection of the estimator structure was guided by the fact that in our application the amount of available samples far exceeded the requirements imposed by resolution constraints.

E. Power Spectrum Estimator Using Bartlett's Procedure

The power spectral density estimates in this article use Bartlett's technique of averaged periodograms, which involves a trade-off between smoothing and spectral resolution. Bartlett's approach can be used to advantage whenever the available record length is so great that the required spectral resolution can be achieved with a small fraction of the available samples. Thus, if the total record length is K but $N \ll K$ samples satisfy the resolution requirements, then $M = K/N$ periodograms may be averaged to obtain a smoothed estimate of the spectral density. Our interest in periodograms stems from the fact that FFTs can be used to compute sampled versions of the desired periodograms quickly and efficiently.

The periodogram $I_N(\omega)$ associated with a sequence $y(n)$ of length N is defined as

$$I_N(\omega) = \frac{1}{N} |\, Y(e^{j\omega})\, |^2 \tag{20a}$$

where

$$Y(e^{j\omega}) = \sum_{n=0}^{N-1} y(n)\, e^{-j\omega n} \qquad \omega = 2\pi f \tag{20b}$$

is the discrete Fourier transform of the sequence $y(n)$. The use of periodograms in spectral estimation can be justified on the grounds that in the limit as N approaches infinity, the expected value of the periodogram approaches the power spectral density of $y(t)$, i.e.,

$$\lim_{N \to \infty} E\,[I_N(\omega)] = S_y(\omega) \tag{21}$$

Thus, in the limit the expected value of the periodogram is the desired power spectral density.

The variance of the periodogram as a function of frequency provides an indication of the amount of random variation about the mean of the estimate. For a real Gaussian sequence with power spectral density $S_y(\omega)$, the covariance is approximately [5]

$$\operatorname{cov}[I_N(\omega_1), I_N(\omega_2)] \cong S_y(\omega_1) S_y(\omega_2) \left\{ \left(\frac{\sin\left[(\omega_1 + \omega_2)\frac{N}{2}\right]}{N \sin\left[\frac{(\omega_1 - \omega_2)}{2}\right]} \right)^2 + \left(\frac{\sin\left[(\omega_1 - \omega_2)\frac{N}{2}\right]}{N \sin\left[\frac{(\omega_1 - \omega_2)}{2}\right]} \right)^2 \right\} \tag{22}$$

Note that the standard deviation of a single periodogram is at least as great as the spectral level itself, at any frequency. At frequencies away from zero, the standard deviation of $I_N(\omega)$ is well approximated by $I_N(\omega)$. Therefore, a single periodogram does not provide a very useful estimate of the power spectral density; hence averaging is usually required to reduce the variance of the spectral estimate.

The FFT can be employed to generate samples of $I_N(\omega)$. With

$$Y(k) \triangleq Y(e^{j\omega})\,|_{\omega = 2\pi k/N}$$

it follows that

$$I_N(k) = I_N(\omega)\,|_{\omega = 2\pi k/N}$$

Since the samples $y(n)$ were assumed to form a Gaussian sequence, it follows that the FFT outputs $Y(k)$ are Gaussian random variables. It is readily demonstrated that the random variables $Y(k)$ are uncorrelated and hence independent by the Gaussian assumption. It follows that the periodogram samples $I_N(k)$ are independent as well.

Let $\hat{S}_y(k)$ denote the final spectral estimate, after averaging over M periodograms. It is evident that

$$\lim_{N\to\infty} E[\hat{S}_y(k)] = \lim_{N\to\infty} \frac{1}{M} \sum_{j=1}^{M} E[I_{N,j}(k)] = S_y(k) \tag{23}$$

$$\operatorname{cov}[\hat{S}_y(k_1), \hat{S}_y(k_2)] \cong \frac{1}{M} S_y^2(k) \left[1 + \delta_{0,k_1}\right] \delta_{k_1,k_2} \tag{24}$$

where δ_{k_1,k_2} is the Kroenecker delta (this function is nonzero only for $k_1 = k_2$, where its value is one). In particular, the variance is

$$\operatorname{var}[\hat{S}_y(k)] = \frac{1}{M} S_y^2(k) \qquad k \neq 0 \tag{25}$$

The spectral estimate samples $\hat{S}_y(k)$ are independent random variables, by virtue of the fact that the final estimate is an average of M random variables. Thus for any k, averaging M independent periodograms reduces the variance of each estimate of spectral density by a factor of M relative to that of a single periodogram.

F. Error Analysis

The estimator described above cannot provide perfect estimates of the desired parameters by processing finite sequences (in fact, no estimator can). We determine the variance of the estimates $\hat{S}_1$ and $\hat{B}_L^*$, under the assumption that enough periodograms were averaged to ensure that the errors in the underlying parameters are but a small fraction of their actual values. Let $\hat{\sigma}_\xi^2$ and $\hat{\sigma}_n^2$ denote the estimates of σ_ξ^2 and σ_n^2, respectively. For small errors, we can write

$$\hat{\sigma}_\xi^2 \cong \sigma_\xi^2 + \epsilon_\xi^2 = \sigma_\xi^2 (1 + x_\xi) \tag{26a}$$

$$\hat{\sigma}_n^2 \cong \sigma_n^2 + \epsilon_n^2 = \sigma_n^2 (1 + x_n) \tag{26b}$$

where

$$x_\xi = \frac{\epsilon_\xi^2}{\sigma_\xi^2} \qquad x_n = \frac{\epsilon_n^2}{\sigma_n^2}$$

Assume that x_ξ and x_n are zero mean random variables, with rms values much less than one. Using Eqs. (18) and (19), the estimates of B_L^* and S_1 can be expressed in terms of their actual values as

$$\hat{B}_L^* = B_L^* \left\{ \frac{1 + x_\xi}{1 + x_n} \right\}^{1/\alpha} \tag{27a}$$

and

$$\hat{S}_1 = S_1 (1 + x_\xi) \tag{27b}$$

The second order statistics of S_1 can be obtained directly:

$$E[\hat{S}_1] = S_1 \tag{28a}$$

$$\text{var}[\hat{S}_1] = S_1^2 \,\text{var}(x_\zeta) = S_1^2 \frac{\text{var}(\hat{\sigma}_\zeta^2)}{\sigma_\zeta^4} \tag{28b}$$

(In fact, these second order statistics for S_1 are valid in general.) To obtain the statistics of $\hat{B}_L^*$, expand the ratio containing the error terms and ignore all but the linear terms:

$$\left\{\frac{1+x_\zeta}{1+x_n}\right\}^{1/\alpha} = \left\{(1+x_\zeta)\left(1-x_n+\frac{x_n^2}{2}-\cdots\right)\right\}^{1/\alpha}$$

$$\cong \left\{1+(x_\zeta - x_n)\right\}^{1/\alpha}$$

$$\cong 1+\frac{1}{\alpha}(x_\zeta - x_n) \tag{29}$$

Thus, for suitably small errors, we obtain the approximation

$$\hat{B}_L^* \cong B_L^* \left\{1+\frac{1}{\alpha}(x_\zeta - x_n)\right\} \tag{30}$$

It follows that

$$E[\hat{B}_L^*] \cong B_L^* \tag{31a}$$

$$\text{var}[\hat{B}_L^*] = \left(\frac{B_L^*}{\alpha}\right)^2 \text{var}(x_\zeta - x_n)$$

$$\leqslant \left(\frac{B_L^*}{\alpha}\right)^2 \left\{\frac{\text{var}(\hat{\sigma}_\zeta^2)}{\sigma_\zeta^4} + \frac{\text{var}(\hat{\sigma}_n^2)}{\sigma_n^4} + 2\frac{\sqrt{\text{var}(\hat{\sigma}_\zeta^2)}\sqrt{\text{var}(\hat{\sigma}_n^2)}}{\sigma_\zeta^2\,\sigma_n^2}\right\} \tag{31b}$$

The upper bound in Eq. (31b) is useful when the correlation between x_ζ and x_n is not well known. Actual numerical values will be determined in the following section, where the techniques for obtaining the parameters from the spectral estimates are examined in greater detail.

III. Pioneer 10 Results

This section presents the results of experiments in tracking the Pioneer 10 spacecraft with the breadboard DSN Advanced Receiver [6]. The data were obtained using the 64 meter antenna at DSS-14 in Goldstone, California. The data include both one-way and three-way transmission modes obtained at various SEP angles, illustrating the effect of the solar corona on carrier phase. Spectra were measured and loop bandwidths were optimized for the various conditions.

The Advanced Receiver is a hybrid analog/digital receiver which makes digital estimates of the carrier phase and filters these estimates with a digital second or third order tracking filter. The filter output drives an analog frequency synthesizer, closing the loop. The phase detector output provides the datastream which is subsequently analyzed to determine the received spectral densities. The power spectral density at the phase detector output, S_y, was obtained as described in Section II.E. These estimates were obtained in near-real time. Phase measurements as a function of time were clocked out of the Advanced Receiver to a control computer, where these measurements were recorded on floppy discs. After sufficient data were recorded, the disc was processed on an IBM PC. The processing was typically completed in less than five minutes, during which time data for the next tracking case was collected by the Advanced Receiver.

A. Spectral Estimation Results

Estimates of the power spectral density of $y(n)$, $\hat{S}_y(k)$, were obtained by means of averaged periodograms, using the FFT. If the sampling rate satisfies the Nyquist criterion, the result is also a good estimate of the spectrum of the continuous process $y(t)$. Results for one-way transmission are shown in Figs. 6a, b, and c. The phase spectral density estimates are represented by the solid curve (the points of the FFT output are connected by straight lines). For the first case, Fig. 6a, the number of points in the sequence was $N = 128$ and $M = 25$ records were averaged. The sampling rate was 8 samples per second. Since for real samples the positive and negative portions of the spectrum are identical, only the positive portion is displayed. For purposes of interpolation, 128 zeros were appended to each record prior to processing, and a 256 point FFT performed (this does not change the total number of independent samples in the FFT output, which remains N). In Fig. 6, a third order loop with parameters $r = 4$, $k = 0.25$ was used, with bandwidths of 0.5 Hz, 0.8 Hz, and 2.0 Hz (the 0.8 Hz bandwidth is nearly optimum). The contribution of the process spectrum near the origin dominates for the 0.5 Hz loop of Fig. 6a; it is still present in the 0.8 Hz loop (Fig. 6b), but is not discernible for the 2.0 Hz loop (Fig. 6c). The dominance of the white noise component is apparent in all cases at frequencies greater than the loop bandwidth.

The above observation suggests the following procedure for estimating the desired components of the spectral density:

(1) Estimate the normalized spectral level $N_0/2A^2$ by averaging the discrete points of the spectral estimate over the upper half of the spectrum. (Henceforth, cap and Est[•] shall both denote "estimate.")

(2) The function $|1 - H(jk)|^2 S_n(k)$ is estimated, assuming the filter transfer function is known.

(3) An estimate of the filtered process spectrum is obtained from Eq. (5b) as

$$\text{Est}\left\{|1 - H(jk)|^2 S_\xi(k)\right\} = \frac{1}{A^2}\left\{\hat{S}_y(k) - |1 - H(jk)|^2 \hat{S}_n(k)\right\} \tag{32}$$

(4) Finally, having decomposed the estimated observation spectral density into its components, estimates of the underlying spectral densities are obtained.

Because the signal amplitude A is assumed known, it follows that

$$\hat{S}_n(k) = A^2\left(\frac{\hat{S}_n(k)}{A^2}\right) \tag{33}$$

Since a $2N$-point FFT was performed on an N-point sequence, the resulting $N/2$-point average has $N/4$ degrees of freedom and hence may be treated as the average of $N/4$ independent random variables. Taking into account the M records that were averaged to obtain the spectral density estimate, the mean and variance of this estimate are

$$E\left[\frac{\hat{S}_n(k)}{A^2}\right] = \frac{N_0}{2A^2} \tag{34}$$

and

$$\text{var}\left[\frac{\hat{S}_n(k)}{A^2}\right] = \frac{4}{NM}\left(\frac{N_0}{2A^2}\right)^2 \tag{35}$$

The smooth dashed curves in Figs. 6a through 6c are the estimates of receiver noise spectra filtered by $(1 - H(jk))$, while the rough dashed curves are the estimates of the filtered phase process spectral density.

The same techniques can be applied to the case of three-way telemetry. Results for three-way tracking on DOY 141 are shown in Fig. 7, again around the optimum loop bandwidth, which in this case was roughly 0.6 Hz. For this day, the SEP angle was 11.8 degrees. This resulted in process noise due to solar scintillation which was almost as high as the one-way phase noise due to the spacecraft oscillator. Estimates of the various system and model parameters can be obtained from these fundamental estimates. The following examples serve to illustrate some techniques for deriving the desired parameter estimates.

B. Phase Error Variance Estimates

The components of the phase error variance can be found from the measured spectra. If the loop bandwidth is known, then from Eq. (15b) the variance of the additive noise component can be found since it is proportional to the normalized noise spectral level estimate:

$$\hat{\sigma}_n^2 = 2B_L\left(\frac{\hat{N}_0}{2A^2}\right) \tag{36a}$$

Using the estimated spectral level, the variance of $\hat{\sigma}_n^2$ is approximately

$$\text{var}(\hat{\sigma}_n^2) \cong \frac{4}{NM}(2B_L)^2\left(\frac{\hat{N}_0}{2A^2}\right)^2 = \frac{4}{NM}(\hat{\sigma}_n^2)^2 \tag{36b}$$

Computation of the variance due to the phase process requires integrating the process spectral estimate. For suitably great N, integration over the lower half of the positive spectrum can be approximated by the sum of independent random variables as

$$\hat{\sigma}_\xi^2 = 2\int_0^\infty |1 - H(j2\pi f)|^2 \hat{S}_\xi(f)\,df$$

$$\cong 2\left\{\Delta f \sum_{k=0,2,4,\cdots}^{\frac{N}{2}-2} |1 - H(jk)|^2 \hat{S}_\xi(k)\right\} \tag{37a}$$

where F is the total frequency range and $\Delta f = F/N$ is the effective spectral resolution of the FFT. Using Eqs. (32) and (35) in Eq. (37a), and since the spectral level estimates obtained from the upper half of the spectrum are independent of the lower half, the variance of the estimate can be expressed as

$$\text{var}(\hat{\sigma}_\xi^2) \cong 4(\Delta f)^2 \left\{ \sum_{k=0,2,4,\cdots}^{\frac{N}{2}-2} \text{var}\left(\frac{\hat{S}_y(k)}{A^2}\right) \right\}$$

$$+ 4(\Delta f)^2 \left(\frac{4}{NM}\right)\left(\frac{\hat{N}_0}{2A^2}\right)^2 \left\{ \sum_{k=0,2,4,\cdots}^{\frac{N}{2}-2} |1 - H(jk)|^2 \right\}^2 \tag{37b}$$

where we used the fact that the $N/2$-point estimate has only $N/4$ degrees of freedom. Near the optimum loop bandwidth the observed spectral level is essentially constant and equal to the normalized spectral level of the additive noise (see Figs. 6 and 7). Upper bounding $|1 - H(jk)|^2$ by one, Eq. (37b) can be approximated as

$$\text{var}(\hat{\sigma}_\xi^2) \cong \frac{4(\Delta f)^2}{M}\left(\frac{N}{4}+1\right)\left(\frac{\hat{N}_0}{2A^2}\right)^2$$

$$= \frac{4(\Delta f)^2}{M}\left(\frac{N}{4}+1\right)\left(\frac{\hat{\sigma}_n^2}{2B_L}\right)^2 \tag{37c}$$

For the Pioneer 10 data obtained on DOY 119 and 141, the total phase error, i.e., the sum of the two components, is plotted as functions of loop bandwidth in Fig. 8, along with error bars of one standard deviation. Both one-way and three-way results are shown. It is apparent that in this case three-way reception is dominated by solar scintillation effects.

C. Optimum Loop Bandwidth

Next we consider the estimation of the optimum loop bandwidth by means of Eq. (18):

$$\hat{B}_L^* = \left[\frac{(\alpha-1)\,\hat{\sigma}_\xi^2}{\hat{\sigma}_n^2}\right]^{1/\alpha} B_L \tag{38}$$

The estimate of the optimum loop bandwidth depends on the ratio of phase process and white noise variances, as well as on the loop bandwidth at which these variances are measured. Table 1 presents the estimated parameters for all data taken during Pioneer 10 tracking. At least three different loop bandwidths were used each day.

The estimates of optimum loop bandwidth are consistent on each day, except for the cases in Table 1 that are flagged by a question mark. These estimates disagree with the other estimates by significantly more than the estimation error. These estimates depend on $\hat{\sigma}_\xi^2$, which is the difference of two relatively large numbers whose difference is small. Thus the actual errors may be dominated by small biases that were not accounted for in the estimation of the larger quantities, one of which is $(N_0/2A^2)$.

In Table 1, the estimate

$$\frac{P_c}{N_0} = \left[2\left(\frac{\hat{N}_0}{2A^2}\right)\right]^{-1} \tag{39}$$

is displayed (in dB-Hz) instead of the normalized noise spectral level, in order to facilitate comparison with standard experimental measurements.

The variances of parameter estimates are displayed in Table 2. These variances were computed using the constant spectral level assumption, and using the parameter estimates instead of their true (but unknown) values in Eqs. (28b) and (31b). Because $\hat{\sigma}_n^2$ and $\hat{\sigma}_\xi^2$ are not highly correlated, we use the approximation $\text{var}(\hat{\sigma}_\phi^2) \cong \text{var}(\hat{\sigma}_n^2) + \text{var}(\hat{\sigma}_\xi^2)$. The variances of $\hat{B}_L^*$ were computed by means of the upper bound in Eq. (31b) and hence tend to be too large. The standard deviation error bars in Figs. 8 and 9 were obtained directly from Table 2. For bandwidths smaller than the optimum, the actual standard deviations may be larger than indicated, because the spectral peak tends to be much greater than the spectral level of the additive noise used in the calculations.

D. Phase Process Spectral Estimates

Estimates of the phase process spectral density at unit frequency S_1 are presented for all of the Pioneer data in Fig. 9 and in Table 1. The spectral density at 1 Hz, S_1, was estimated by means of Eq. (19). The f^{-3} model was used for all one-way data, and the $f^{-8/3}$ model was used for all three-way data. The SEP angle is indicated in Fig. 9 for each day data was collected. The results show that one-way data have spectral levels of $S_1 = 1$ to 2×10^{-3} r^2/Hz.

For the three-way data, the results depend on SEP angle, indicating that here solar scintillation effects dominate. The measured spectral levels were approximately 10^{-4} r^2/Hz on DOY 128, when the SEP angle was 23.7 deg, and 10^{-3} r^2/Hz on DOY 141 at an SEP angle of 11.8 deg. Armstrong, Woo, and Estabrook [1] have measured solar scintillation dominated carrier spectra using the Viking spacecraft. At $f = 0.001$ Hz, they observed a spectral level of 10^3 to 10^5 r^2/Hz at 23.7 deg

and 10^4 to 10^6 r^2/Hz at 11.8 deg for one-way paths at a carrier frequency of 2.3 GHz. Multiplying by 10^8 to convert to S_1 using the $\alpha = 8/3$ assumption, and also multiplying by 2 to convert to three-way reception, the corresponding range for S_1 becomes 2×10^{-5} to 2×10^{-3} at 23.7 deg and 2×10^{-4} to 2×10^{-2} at 11.8 deg. Although extrapolation to frequencies as high as 1 Hz may not be accurate, we observe that our results are consistent with the previously measured values. The variation in the S_1 estimates evident in the three-way mode (Fig. 9) could be the result of actual solar scintillation, or could be due to modeling errors. For example, during three-way reception, the phase noise is due to a combination of spacecraft transmitter phase effects and solar scintillation; hence the effective exponent α may not be exactly 8/3, as was assumed in the calculations. In addition, the loop bandwidth in the Advanced Receiver is not precisely known. The estimates of S_1 are sensitive to both of these effects. However, since loop bandwidth optimization is less critically dependent on B_L and α, our model is sufficiently accurate for the purpose of optimizing receiver loop bandwidth. Since the spectra measured in [1] tend to exhibit significant fluctuations, our method of measuring spectra in real time should prove to be very useful for optimizing loop bandwidths and for obtaining other useful system parameter estimates during telemetry.

IV. Conclusions

A method for optimizing loop bandwidths via spectral estimation for phase locked loop receivers has been developed and used to improve carrier tracking for the Pioneer 10 spacecraft. Estimates were made of the relevant spectral parameters and of the total noise power for one-way and three-way transmission, and the variance of the phase error in the loop was minimized. Results obtained in the field were found to be in good agreement with theoretical values. In addition, by analyzing phase spectra, solar channel effects were detected and compensated for. Thus the Fourier analysis of the phase detector output was shown to be an important tool which in addition to bandwidth optimization can be used to monitor channel effects, transmitted carrier stability, and make estimates of relevant system parameters.

It was specifically shown for Pioneer 10 that receiver loop bandwidths of 0.1 to 1.0 Hz are feasible, depending on the type of transmission (one-way or three-way), and depending on the SEP angle. When compared to the 3 Hz loop bandwidths used with operational DSN receivers, it is clear that the narrower loop bandwidths achieve improvements of 5 to 15 dB in carrier tracking threshold and carrier loop SNR.

References

[1] J. W. Armstrong, R. Woo, and F. B. Estabrook, "Interplanetary Phase Scintillation and the Search for Very Low Frequency Gravitational Radiation," *The Astrophysical Journal*, vol. 230, pp. 570-574, June 1, 1979.

[2] S. Aguirre and W. J. Hurd, "Design and Performance of Sampled Data Loops for Subcarrier and Carrier Tracking," *TDA Progress Report 42-79*, vol. July-September 1984, Jet Propulsion Laboratory, Pasadena, California, pp. 81-95, November 15, 1984.

[3] R. Gagliardi, *Introduction to Communications Engineering*, New York: John Wiley & Sons, 1978.

[4] D. Halford, "A General Mechanical Model for $|f|^{\alpha}$ Spectral Density Random Noise with Special Reference to Flicker Noise $1/|f|$," *Proc. IEEE*, vol. 56, pp. 251-258, March 1986.

[5] A. V. Oppenheim and R. W. Schafer, *Digital Signal Processing*, New York: Prentice-Hall, 1975.

[6] D. H. Brown and W. J. Hurd, "DSN Advanced Receiver: Breadboard Description and Test Results," *TDA Progress Report 42-89*, vol. January-March 1987, Jet Propulsion Laboratory, Pasadena, California, pp. 48-66, May 15, 1987.

Table 1. Parameter estimates

DOY	GMT	B_L (Hz)	SEP	$\left(\frac{\widehat{P_c}}{N_0}\right)$ (dB–Hz)	$\widehat{\sigma_\xi^2}$ ($\times 10^{-2}$)	$\widehat{\sigma_n^2}$ ($\times 10^{-2}$)	$\widehat{\sigma_\phi^2}$ ($\times 10^{-2}$)	$\widehat{B_L^*}$ (Hz)	$\widehat{S}_1$ ($\times 10^{-4}$)	
119	2:39	0.5		11.6	7.79	3.44	11.23	0.83	10.7	
119	2:02	0.7	32.4°	12.0	4.42	4.42	8.84	0.88	11.9	
119	3:32	0.8		10.6	3.17	6.91	10.08	0.78	11.2	
119	4:03	1.0		9.8	3.91	10.4	14.31	0.91	21.5 ?	One Way
140	22:14	0.5		13.2	8.76	2.41	11.17	0.97	12.1	
140	22:46	0.8	11.8°	13.5	3.07	3.60	6.67	0.96	10.8	
140	22:30	2.0		12.2	2.07	12.2	14.27	1.40	45.6 ?	
128	3:04	0.125		12.6	5.25	0.69	5.94	0.32	1.40	
128	3:25	0.25	23.7°	11.8	1.29	1.65	2.94	0.28	1.09	
128	2:42	0.5		12.6	0.81	2.74	3.55	0.38	2.2	
141	1:30	0.25		12.3	8.55	1.46	10.01	0.59	7.2	Three Way
141	1:55	0.375		11.9	5.43	2.40	7.83	0.62	9.0	
141	0:51	0.5	11.8°	12.6	3.28	2.75	6.03	0.65	8.8	
141	0.12	0.75		12.9	2.33	3.87	6.20	0.75	12.3	
140	23:32	1.0		12.7	1.75	5.44	7.19	0.79	14.9	

Table 2. Variances of parameter estimates

DOY	B_L (Hz)	$\text{var}\left(\frac{\widehat{N_0}}{2A^2}\right)$ ($\times 10^{-7}$)	$\text{var}(\widehat{\sigma_\phi^2})$ ($\times 10^{-6}$)	$\text{var}(\widehat{S}_1)$ ($\times 10^{-9}$)	$\text{var}(\widehat{B_L^*})$ ($\times 10^{-4}$)	
119	0.5	5.1	8.9	1.6	2.6	
119	0.7	4.3	7.9	5.1	5.7	
119	0.8	16	31	33	25	
119	1.0	34	69	170	47	One Way
140	0.5	7.3	13	2.3	5.8	
140	0.8	4.4	8.4	9	14	
140	2.0	8.1	26	650	92	
128	0.125	7.4	3.1	0.02	0.61	
128	0.25	5.2	2.3	0.15	2.0	
128	0.5	19	9.9	5.7	33	
141	0.25	7.4	3.2	0.22	1.2	Three Way
141	0.375	8.9	4.2	1.0	2.2	
141	0.5	3.9	2.0	1.2	2.2	
141	0.75	2.1	3.9	9.5	7.5	
140	1.0	2.3	4.7	28	15	

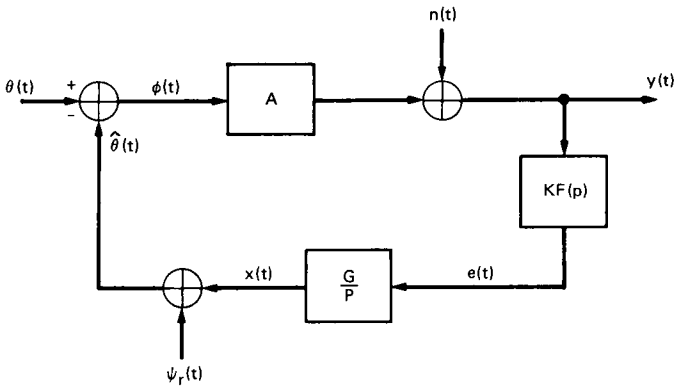

Fig. 1. Receiver phase locked loop block diagram

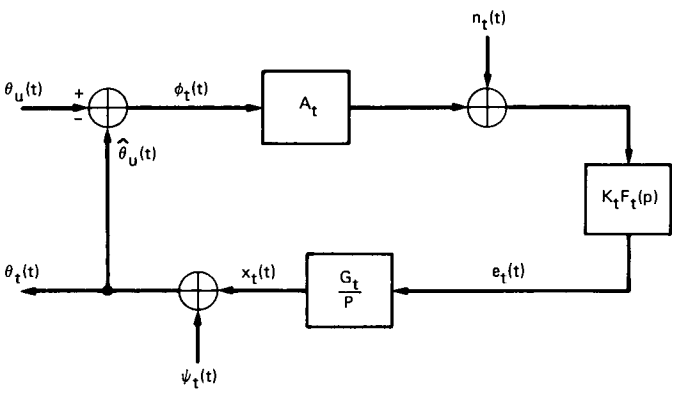

Fig. 2. Spacecraft transmitter phase locked loop block diagram

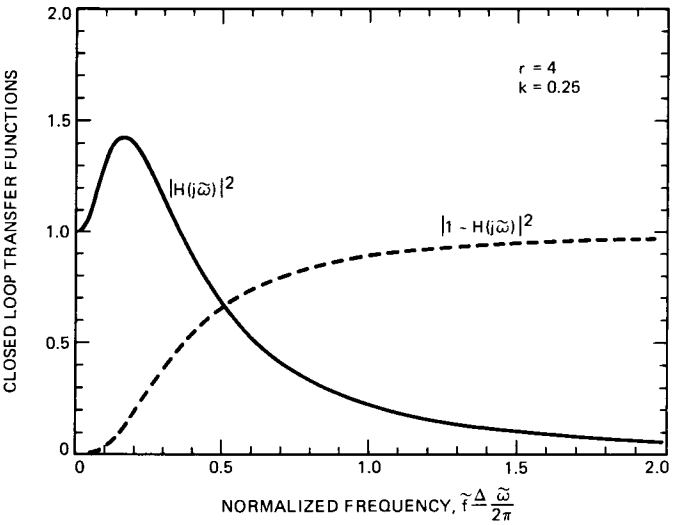

Fig. 3. Normalized closed loop transfer functions

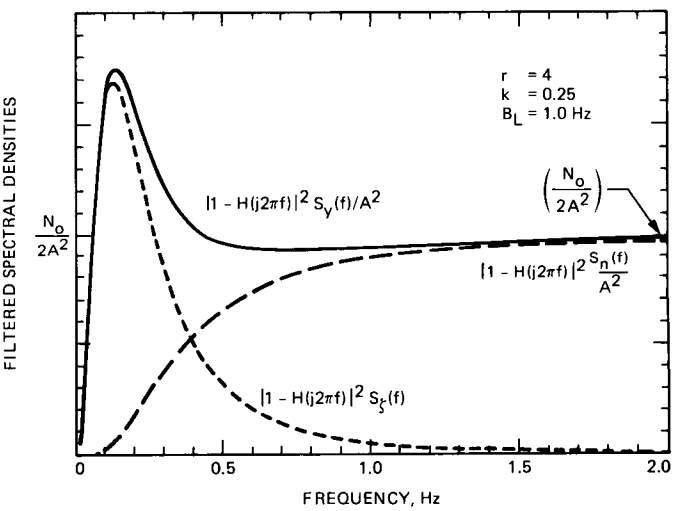

Fig. 4. Filtered spectral densities for a third order loop (inverse f^3 phase process and additive white noise)

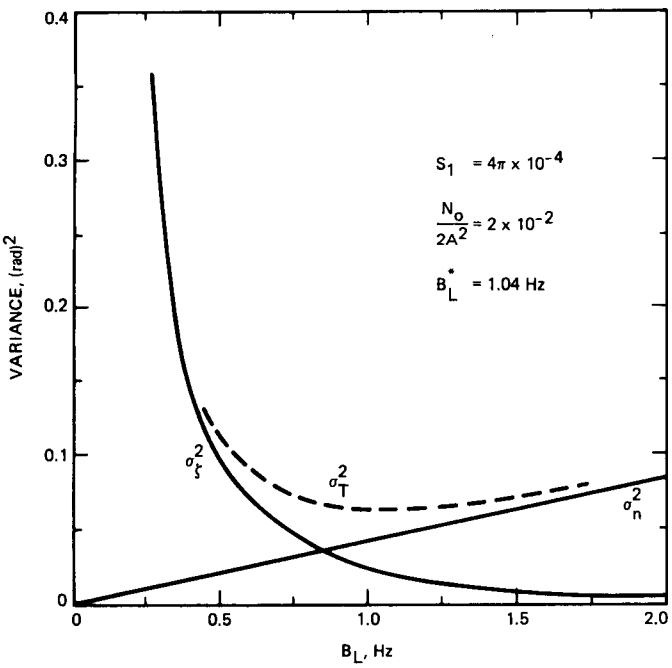

Fig. 5. Phase error variance and components as a function of loop bandwidth ($\alpha = 3$)

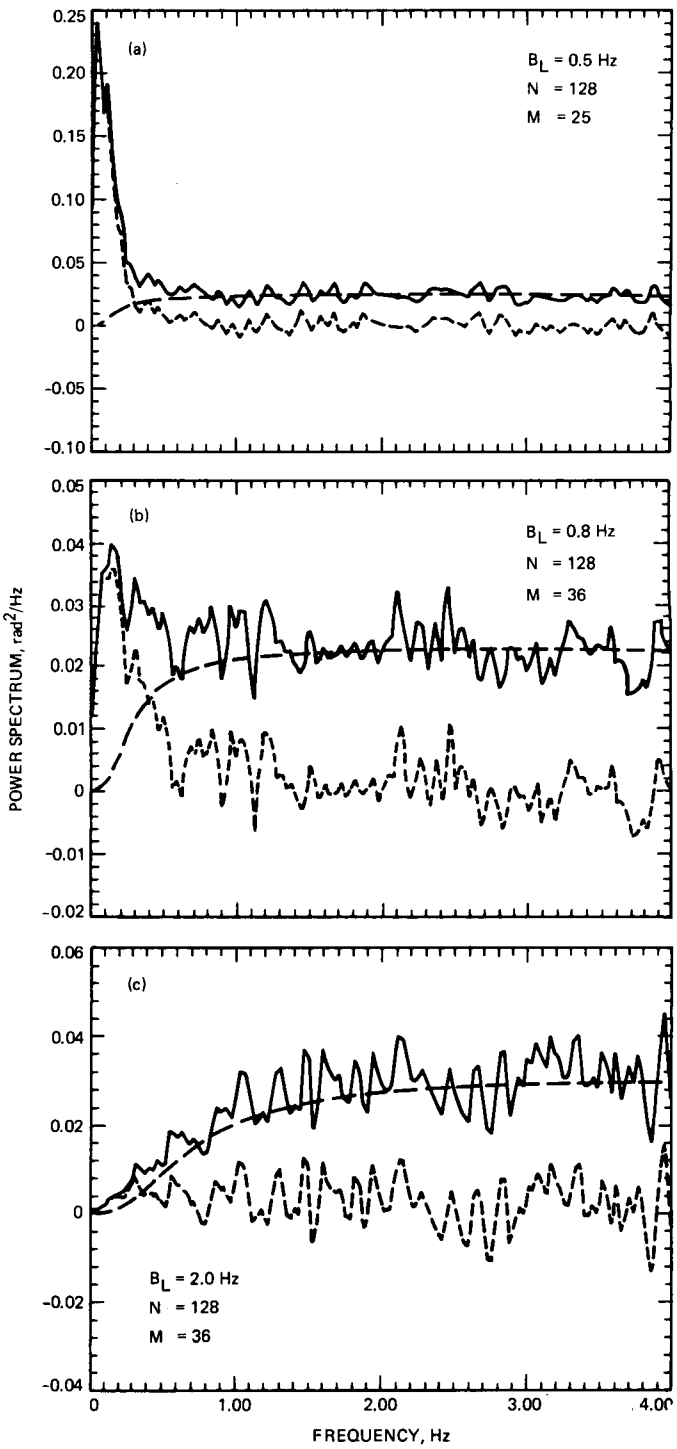

Fig. 6. Spectral density estimates (one-way mode)

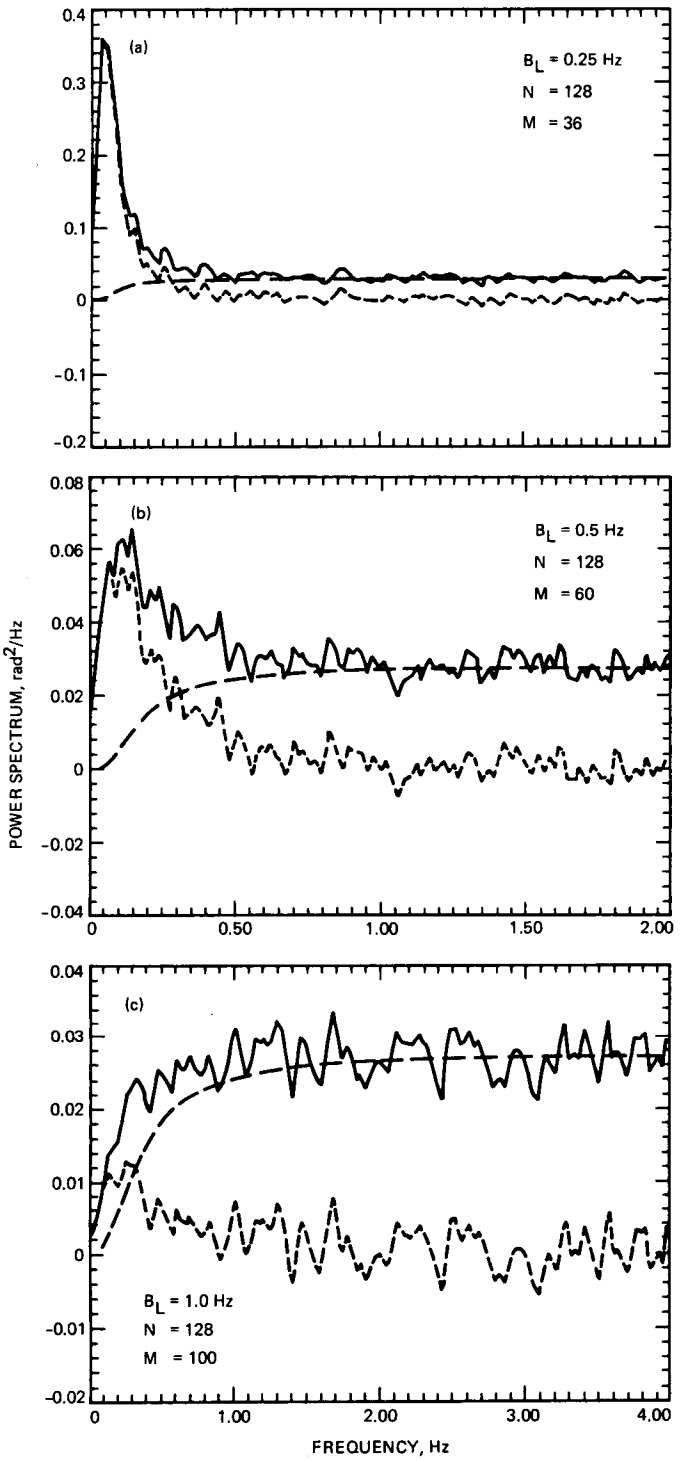

Fig. 7. Spectral density estimates (three-way mode)

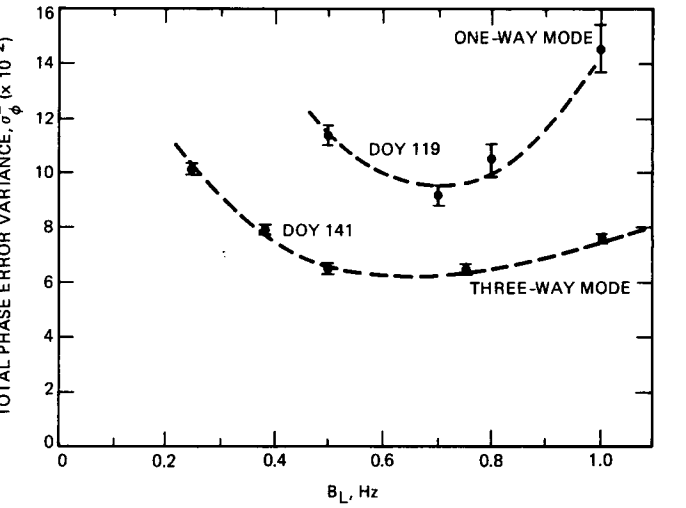

Fig. 8. Measured total phase error variances as a function of loop bandwidth

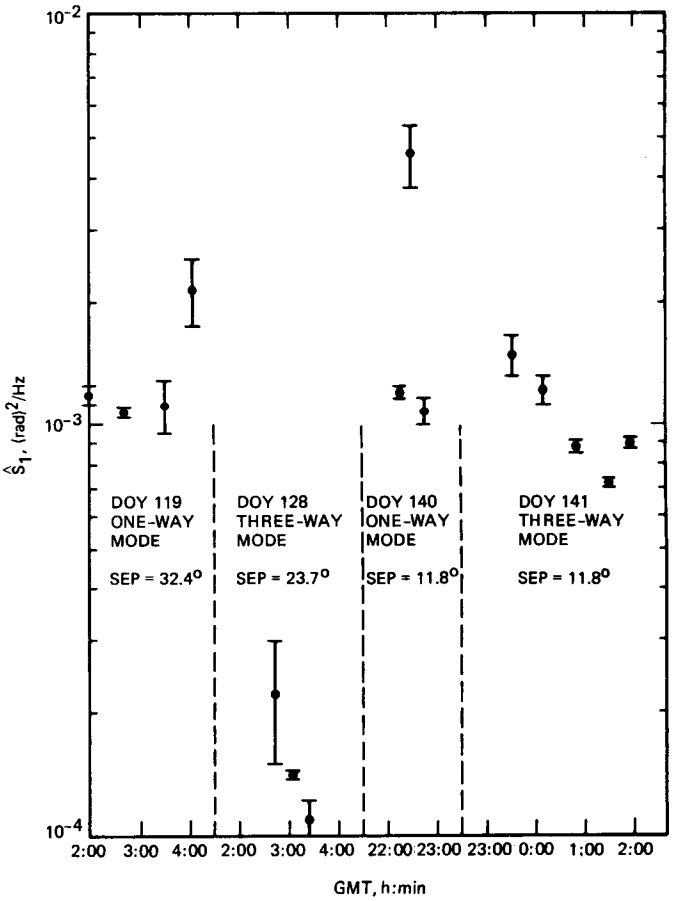

Fig. 9. Estimates of phase spectrum parameter

Appendix

Maximum of Filtered Spectrum

Here we demonstrate that for f^{-3} type phase processes the maximum of the filtered process spectrum $|1 - H(j\,2\pi f)|^2 S_\xi(f)$ is always at a given fraction of the loop bandwidth, for transfer functions of the form defined in Eq. (7) and inverse f^3 process spectrum defined in Eq. (11). These functions can be expressed in terms of the radian frequency $\omega = 2\pi f$ as

$$S_\xi(\omega) = (2\pi)^3 \frac{S_1}{|\omega|^3} \tag{A1}$$

and

$$|1 - H(j\omega)|^2 S_\xi(\omega) = (2\pi)^3 S_1 G(\omega; r, k, \tau_2) \tag{A2}$$

where

$$G \triangleq \omega^3 [\omega^6 + \alpha_1 \omega^4 + \alpha_2 \omega^2 + \alpha_3]^{-1}$$

$$\alpha_1 = \frac{r(r-1)}{\tau_2^2} \qquad \alpha_2 = \frac{r^2(1-2k)}{\tau_2^4} \tag{A3}$$

$$\alpha_3 = \frac{r^2 k^2}{\tau_2^6}$$

Setting $y = \omega^2$, differentiating Eq. (A3) with respect to y, and setting the result equal to zero yields the cubic equation

$$y^3 + \left(\frac{\alpha_1}{3}\right) y^2 - \left(\frac{\alpha_2}{3}\right) y - \alpha_3 = 0 \tag{A4}$$

Further, letting $x = y + (\alpha_1/9)$ results in the simplified form

$$x^3 + ax + b = 0 \tag{A5}$$

where

$$a = \frac{1}{3}\left(-\alpha_2 - \left(\frac{\alpha_1^2}{9}\right)\right) \tag{A6a}$$

$$b = \frac{1}{27}\left(2\frac{\alpha_1^3}{27} + \alpha_1\alpha_2 - 27\alpha_3\right) \tag{A6b}$$

Trigonometric solutions for x are obtained by letting $x = m\cos\theta$, with $m = 2\sqrt{-a/3}$. The solutions for y are of the form

$$y_i = (2\pi)^2 C_i^2 (r, k) B_L^2 \tag{A7}$$

Taking only the positive solutions, we obtain

$$\omega^* = 2\pi C_0(r, k) B_L \tag{A8}$$

Direct evaluation yields the location of the maxima for $r = 4$

$$k = 0: \; f^* = C_0(4, 0) B_L = 0.147 B_L \tag{A9a}$$

$$k = 0.25: \; f^* = C_0(4, 0.25) B_L = 0.127 B_L \tag{A9b}$$

These results are confirmed by the graphs shown in Fig. A1, where the location of the maxima are seen to be at the predicted frequencies. This property helps to determine if the observed phase process is indeed an f^{-3} type process.

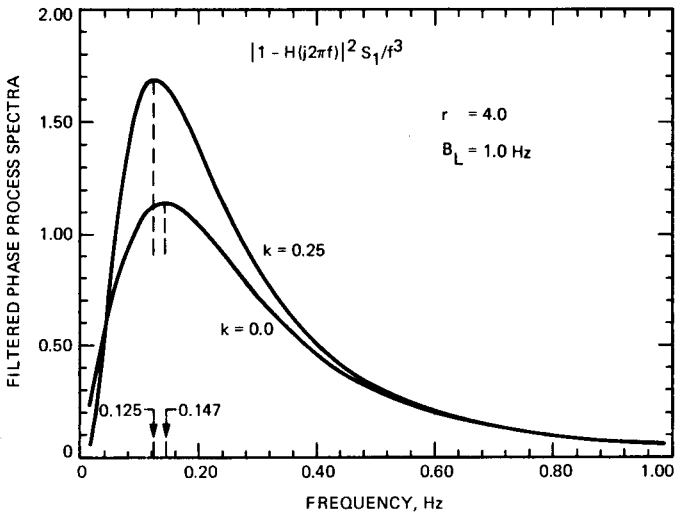

Fig. A1. Filtered process spectra for second and third order loops